*Malaysian Journal of Chemistry, 2025, Vol. 27(3), 242-253*
(Special Issue: *2nd International Science and Technology Colloquium, i-COSTECH 2024*)

# Exploring the Properties and Photocatalytic Performance of Ag/AgI/g-$C_3N_4$ Composite for Methylene Blue Degradation

**Rozaina Saleh[1,2], Nurul IzzaTaib[2]*, Zakiah Mohamed[1], Mohd Lokman Ibrahim[1] and Nasr Bensalah[3]**

[1]School of Chemistry and Environment, Faculty of Applied Sciences, Universiti Teknologi MARA, 40450 Shah Alam, Selangor, Malaysia

[2]Faculty of Applied Sciences, Universiti Teknologi MARA Perak Branch, Tapah Campus, 35400 Tapah Road, Perak

[3]Department of Chemistry and Earth Sciences, College of Arts and Science, Qatar University, P.O. Box 2713, Doha, Qatar

*Corresponding author (e-mail: izza257@uitm.edu.my)

Dye pollution from industrial wastewater poses a significant threat to aquatic ecosystems, necessitating efficient removal strategies. Photocatalysis, which employs material such as graphitic carbon nitride (g-$C_3N_4$), has emerged as a viable strategy for degrading organic compounds. In this study, visible light active, Ag/AgI/g-$C_3N_4$ composite photocatalysts were fabricated via in-situ co-precipitation method with different AgI percent weight loading. Detail characterization was performed utilizing a variety of approaches. The incorporation of Ag/AgI into the g-$C_3N_4$ extends the visible light absorption range, contributing to improved photocatalytic activity. The Ag/AgI/g-$C_3N_4$ composite outperformed the pristine g-$C_3N_4$ in terms of methylene blue degradation. The optimal photocatalytic activity was observed by 1AgI/g-$C_3N_4$ photocatalyst with 1% AgI loading, achieving 80% degradation in 5 hours due to the reduced electron-hole recombination and efficient charge transfer between g-$C_3N_4$ and Ag/AgI particles.

**Keywords**: Photocatalyst; photocatalysis; graphitic carbon nitride; silver iodide; methylene blue

*Received: October 2024; Accepted: December 2024*

The discharge of dye-contaminated wastewater leads to the pollution of soil, groundwater, and surface water. Methylene Blue (MB) is a well-known cationic dye that is linked to a variety of health problems, including vomiting, eye burns, nausea, jaundice, difficulty breathing, and cancer [1]. Traditional water treatment technologies, such as physical sedimentation, chemical oxidation, and biodegradation, are no longer capable of meeting increasingly severe environmental quality standards due to the high stability and complex structure of dyes [2].

Silver halides (AgX), such as silver iodide (AgI) photocatalysts, have gained attention for their high efficiency in degrading a wide range of pollutants [3]. The visible-light range band gap of the AgI nanostructures makes it suitable for photocatalysis. Additionally, the excellent conductivity of AgI aids in electron transfer and minimizes electron-hole recombination [4]. However, AgI is prone to degradation into Ag under light exposure, thus limiting its photocatalytic applications [5]. Therefore, methods to improve AgI stability and prevent photocorrosion are needed. Recent studies have demonstrated that dispersing AgI on support materials enhances its stability by improving electron-hole separation. As a result, various AgI-based composite photocatalysts have been manufactured, including AgI/$TiO_2$, Ag-AgI/$Fe_3O_4$@$SiO_2$, GO/AgI/$Bi_2O_3$, and [6–9]. The AgI supported photocatalysts were reported to display substantial photocatalytic performance, resulting from the creation of the heterojunction between the AgI and supporting materials. However, the localized surface plasmon resonance (LSPR) characteristic of the Ag metal gives it special optical features. LSPR significantly enhances visible-light absorption, which is crucial for the advancement of plasmonic photocatalysts. Furthermore, the LSPR effect is closely influenced by the medium surrounding the metallic Ag. The combination of Ag and AgI with correct support has been reported to boost the photocatalytic ability of the photocatalysts [10, 11].

Graphitic carbon nitride (g-$C_3N_4$), a polymer-like semiconductor composed of non-metals, has attracted significant attention in recent years due to its non-toxic nature, ability to be activated by visible light, and ideal band gap energy [12]. The adjustable band gap of g-$C_3N_4$ promotes its versatility for doping and forming heterojunctions with other semiconductors, enabling improvements in its photocatalytic performance and broadening its application range [13]. However, the application of g-$C_3N_4$ as a photocatalyst is constrained by its limited light absorption range and

†Paper presented at the 2nd International Science and Technology Colloquium (i-COSTECH 2024)

the rapid recombination of photoinduced electron-hole pairs [14]. Thus, the combination of g-$C_3N_4$ with other semiconductor or metallic materials has been widely employed to improve light absorption and reduce the recombination rate [15]. For example, g-$C_3N_4$ doped with P and Cl [16], modified g-$C_3N_4$ $ZnFe_2O_4$, $CoFe_2O_4$ supported on N-doped graphene [17], copper doped porous g-$C_3N_4$ by template-mediated approach [18], $CeO_2$/N-doped on g-$C_3N_4$ [19] and magnetic $CuNiFe_2O_4$/g-$C_3N_4$ were found to show enhanced photocatalytic activity in degrading the target pollutants. According to earlier research, the incorporation of semiconductor or other metal on the g-$C_3N_4$ enhances its ability to trap electrons during photocatalytic charge separation, which slows down electron-hole recombination [20–22]. Leveraging the prior research, the combination of g-$C_3N_4$ with Ag/AgI may substantially improve the photocatalytic efficacy of the photocatalyst. This enhancement corresponds to the increased visible-light absorption of AgI, the effective electron-hole separation offered by g-$C_3N_4$, and the LSPR effect of the Ag metal. Additionally, the heterojunction formed between these materials promotes better charge transfer and minimizes photo corrosion, resulting in a more efficient and durable photocatalyst.

Therefore, we present a simple one-pot precipitation approach for producing Ag/AgI/g-$C_3N_4$ composite photocatalyst. The characteristics of the Ag/AgI/g-$C_3N_4$ composites were then investigated using various physical techniques. Finally, the photocatalytic ability of the Ag/AgI/g-$C_3N_4$ composite to degrade methylene blue (MB) dye upon visible light illumination will be tested and evaluated.

## EXPERIMENTAL

### Chemicals and Materials

Distilled water (DW), Urea ($CH_4N_2O$, 99%), ethanol absolute ($C_2H_6O$), silver nitrate ($AgNO_3$, 99%) sodium iodide (NaI, 99%), and methylene blue ($C_{16}H_{18}ClN_3S$).

### Synthesis of g-$C_3N_4$

To synthesize g-$C_3N_4$, a thermal polymerization process was utilized with urea as a starting material. Urea (10 g) was heated at 550 °C in a muffle furnace for 3 hours. The substance was ground into a fine powder and kept for later use, denoted as g-$C_3N_4$, once it cooled to room temperature.

### Synthesis of Ag/AgI/g-$C_3N_4$ Composite

AgI/g-$C_3N_4$ composite photocatalysts were synthesized by a one-pot in-situ precipitation method. 0.5 grams of g-$C_3N_4$ were mixed with 100 mL of distilled water and then subjected to ultrasonication for 30 minutes. 10 mL aqueous $AgNO_3$ with a particular concentration was added to the mixture and agitated for 120 minutes under dark conditions. Afterward, 10 mL of NaI aqueous solution was added drop by drop and agitated for 2 hours, followed by irradiation with a Hg lamp for 30 minutes with stirring. The resulting precipitate was centrifuged, washed, and then dried in an oven at 60°C for 24 hours. According to this method, different weight percentages of AgI to g-$C_3N_4$/$Fe_3O_4$ (1%, 10%, and 50%) photocatalysts were obtained and denoted as 1Ag/AgI/g-$C_3N_4$, 10Ag/AgI/g-$C_3N_4$, and 50Ag/AgI/g-$C_3N_4$ respectively. **Figure 1** shows the Ag/AgI/g-$C_3N_4$ composite photocatalyst preparation scheme.

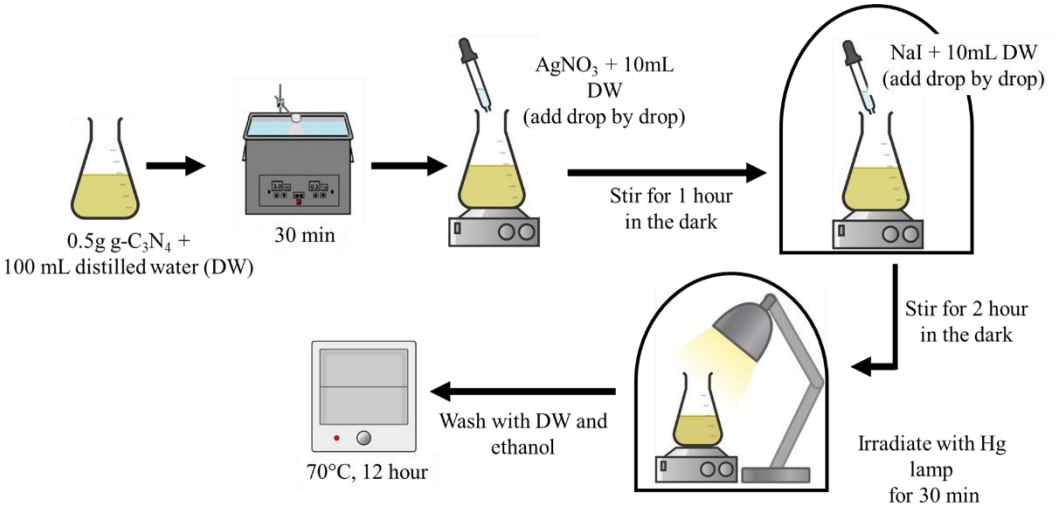


**Figure 1.** The synthesis procedure of fabricating the Ag/AgI/g-$C_3N_4$ composite.

### Characterization of Samples

X-ray diffraction (XRD) analysis was conducted using a PANanalytical X'pert Pro Model PW3040. Fourier transform infrared (FTIR) spectra were acquired using a Perkin Elmer Spectrum One FTIR spectrophotometer. The band gap of photocatalysts was evaluated using the Lambda 950, a PerkinElmer UV–Vis–NIR. The scanning wavelength was adjusted between 300 and 900 nm using tungsten-halogen and deuterium lamps. The Bruker-Zeiss FESEM with QUANTAX EDS was employed to examine particle surface morphology and distribution at a 15 kV accelerating voltage. HRTEM analysis was conducted at 200kV using a Tecnai G2 20 S-TWIN Transmission Electron Microscope (TEM). Elemental analysis and purity of the products were both determined utilizing EDX on a similar FESEM instrument. Shimadzu AXIS Ultra DLD spectrometer Kratos was employed for X-ray photoelectron spectroscopy (XPS).

### Photocatalytic Activity

Photocatalysis experiments were conducted in a 200 mL cylindrical double-jacketed beaker outfitted with a water circulation system. The solution was magnetically agitated and consisted of 0.1 g of photocatalyst and 100 mL of MB solution. To establish adsorption equilibrium, the solution was constantly agitated for 60 minutes in the dark. At regular intervals, 3 mL of the reaction samples were obtained from the beaker, and the photocatalyst was filtered prior to UV-Vis spectrophotometer (Perkin Elmer/ Lambda 25) examination at 664 nm, which corresponded to the maximum absorption wavelengths of MB. The percent degradation (% degradation) was determined as follow: % degradation = $[(C_0 - C_t]/C_0\ x\ 100$, $C_0$ and $C_t$ is the initial concentration, and $C_t$ is the final concentration of the dye, respectively.

## RESULTS AND DISCUSSION

### Characterization of the Photocatalysts

The structural characteristics of g-$C_3N_4$ and all Ag/AgI/g-$C_3N_4$ composite photocatalysts were examined using Fourier-transform infrared (FTIR) spectra, as shown in **Figure 2**.

The less intense peaks at 812 $cm^{-1}$ correspond to the breathing mode of tri-s-triazine, a six-membered heterocyclic ring that is present in the g-$C_3N_4$ structure [23], while the peak at 890 $cm^{-1}$ is attributed to the N-H bonds deform in a cross-linked manner [24]. These peaks are specific characteristics of g-$C_3N_4$ and are typically observed in its FTIR spectra [25]. Peaks in the 1200–1600 $cm^{-1}$ range, present in both g-$C_3N_4$ and Ag/AgI/g-$C_3N_4$ samples, corresponding to the stretching vibrations of CN heterocyclic compounds [26], primarily attributed to the tri-s-triazine ring and imine (C=N) group [27]. The peaks at 1245 $cm^{-1}$ and 1322 $cm^{-1}$ reflect the out-of-plane bending vibrations, which are characteristic of heptazine rings [28]. Additionally, the broad bands observed in the range of 3100-3450 $cm^{-1}$ are attributed to the stretching vibrations modes of N-H groups of the g-$C_3N_4$ aromatic rings, and O-H bands attributable to adsorbed water molecules [29]. Tran et al. [30] and Morsy et al. [31] reported a similar finding in their analysis of g-$C_3N_4$ structures, thus further supporting the characteristics feature of g-$C_3N_4$. No distinct absorption peaks for AgI were observed, likely due to its transparency in the mid-infrared region, as reported previously [32].

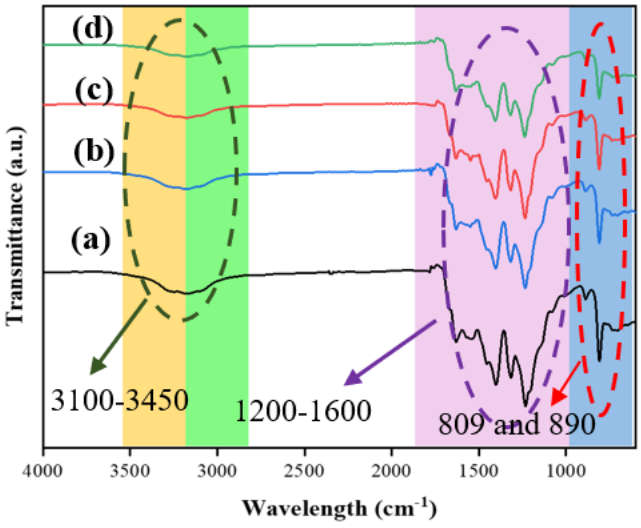


**Figure 2.** FTIR spectra of (a) g-$C_3N_4$ (b) 1Ag/AgI/g-$C_3N_4$ (c) 10Ag/AgI/g-$C_3N_4$ (d) 50Ag/AgI/g-$C_3N_4$.

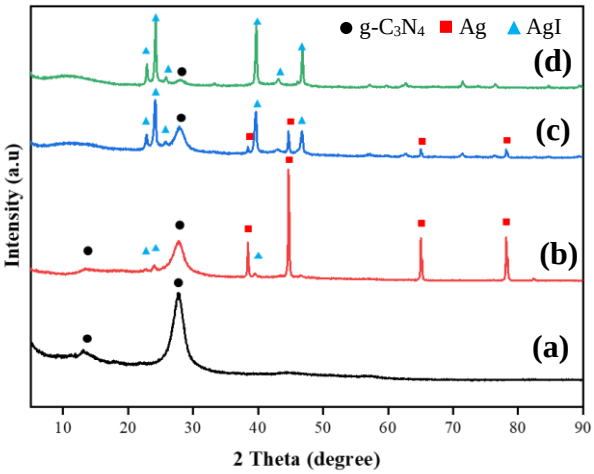


**Figure 3.** XRD patterns of (a) g-$C_3N_4$ (b) 1Ag/AgI/g-$C_3N_4$ (c) 10Ag/AgI/g-$C_3N_4$ (d) 50Ag/AgI/g-$C_3N_4$.

The X-ray diffraction (XRD) patterns of the g-$C_3N_4$ and all Ag/AgI/g-$C_3N_4$ with varying AgI loadings are presented in **Figure 3**.

The sharp and intense peak around 27.6° in the XRD pattern of the g-$C_3N_4$ sample is attributed to the (002) interlayer stacking reflection of the conjugated aromatic segments plane, indicating a layered structure consistent with the hexagonal symmetry of the crystal framework [33]. Moreover, a weaker peak at 13.2° is observed, associated to the (100) in-plane structural packing repeating motif of the tri-s-triazine unit, which is composed of one-dimensional (1D) melon strands (JCPDS 87-1526) [34]. Due to the amorphous nature of the material, the g-$C_3N_4$ peaks are relatively broad. These characteristic diffraction patterns affirm the successful synthesis of the g-$C_3N_4$ via the thermal polymerization method. A similar phenomenon has been observed in previous studies [35,36]. The XRD patterns of Ag/AgI/g-$C_3N_4$ composites with various AgI loadings displayed distinct peaks of g-$C_3N_4$ at the (002) and (100) planes, although these peaks showed reduced intensity. For 1Ag/AgI/g-$C_3N_4$ composite, distinct peaks at 2θ = 38.1°, 44.1°, 64.4°, 77.3°, and 81.3° were identified, corresponding to the (111), (200), (220), (311), and (222) lattice planes of the face-centered cubic structure of Ag crystals (JCPDS No. 65-2871), indicating the dispersion of Ag particles in the composite [37]. Furthermore, small peaks at 2θ = 22.87°, 24.06° and 39.5° were observed. These are ascribed to the (100), (002), and (110) AgI planes in accordance with JCPDS no. 09-0374 [38]. For the 10Ag/AgI/g-$C_3N_4$ composite, the peaks corresponding to Ag crystals show a decrease in intensity, while clear and distinct peaks for AgI are observed at the (100), (002), (101), (110), (103), and (112) planes, confirming the successful formation of AgI in the structure. The XRD pattern for 50Ag/AgI/g-$C_3N_4$ composite reveals no peaks corresponding to Ag crystals, indicating the absence or low concentration of Ag particles. Notably, peaks at 2θ = 22.87°, 24.06° and 25.86° are attributed to the (100), (002), (101) planes, while peaks at 39.73°, 43.16°, and 46.87° are assigned to (110), (103), and (112) planes of AgI, respectively. Apparently, the intensity of AgI peaks becomes more pronounced with an increase in the weight percentage of AgI, while the Ag and g-$C_3N_4$ peaks gradually diminish in intensity. Meanwhile, characteristic diffraction peaks of AgI are consistent with those reported in the previous literature [32,35]. This phenomenon occurs because, at low AgI concentrations, Ag atoms may disperse on the g-$C_3N_4$ surface or form small clusters. Upon irradiation with Hg lamp, $Ag^+$ ions are reduced to Ag particles, which contributes to the peaks observed in the XRD diffractogram. However, the high availability of $Ag^+$ ions promotes the formation of AgI crystals rather than Ag clusters when the AgI concentration increases. This transition may be driven by changes in the AgI-to-Ag ratio or alterations in reaction kinetics.

FESEM and TEM techniques were employed to examine the morphology and microstructure uniformity of the synthesized photocatalyst. From **Figure 4(a)**, the g-$C_3N_4$ exhibits loose sheets, lightweight, and fluffy characteristics, which can be due to the substantial emission of $NH_3$ gas during the calcination process. As for the Ag/AgI/g-$C_3N_4$ composite samples (**Fig. 4(b)-(d)**), the AgI nanoparticles were evenly distributed across the g-$C_3N_4$ surface, forming heterostructures. As the AgI content increased, the AgI stacking on the g-$C_3N_4$ surface became more prominent, resulting in agglomeration of the particles, similar to previous studies [39]. **Figure 4(e)** shows the TEM images of the 10Ag/AgI/g-$C_3N_4$ sample. The TEM image shows sphere shape Ag/AgI nanoparticles, with an average diameter of approximately 10

nanometers, are homogeneously distributed on the lamellar surface of the g-$C_3N_4$ sheet. TEM image also reveals the profound contact between AgI and g-$C_3N_4$ has been successfully created. This intact produced a heterojunction system, which could offer more photocatalytic reaction sites, thereby enhancing the overall photocatalytic performance. The HRTEM image in **Figure 4(f)** further verifies the development of a heterostructure in the 10AgI/g-$C_3N_4$ composite. The lattice fringes observed include 0.206 nm for Ag, corresponding to the (200) plane [40], and 0.230 nm for AgI corresponding to the (220) plane [41]**.**

The UV-vis DRS spectra show the optical characteristics of all photocatalysts (**Figure 5(a)**). All Ag/AgI/g-$C_3N_4$ composite photocatalysts demonstrated significant absorption of visible light, with absorption edges similar to g-$C_3N_4$ alone. As the loading of AgI increased, a slight red-shift in the adsorption edge of Ag/AgI/g-$C_3N_4$ composites was observed, attributed to the localized surface plasmon resonance (LSPR) effect of metallic Ag nanoparticles on the Ag/AgI/g-$C_3N_4$ composite surface [42]. This finding suggests that Ag/AgI/g-$C_3N_4$ composites will perform better as photocatalysts when irradiated with visible light. This finding suggests that Ag/AgI/g-$C_3N_4$ composites will perform better as photocatalysts when irradiated with visible light [43]. The UV-vis DRS data for the optical absorbance of the synthesized photocatalysts were used to estimate the band gap energy, employing the Tauc equation presented in Equation (1) [44].

$$(\alpha h\nu)2 = K(h\nu - Eg) \quad (1)$$

where α is the absorption coefficient, hν is the photon energy, $E_g$ is the optical bandgap energy, and K is a constant related to the material's electronic and structural properties. The Tauc plot plots $(\alpha h\nu)^2$ against photon energy (hν). The Tauc plot comprises a straight line with a gradient of $-1/E_g$ and an intercept of $K(E_g)^2$.

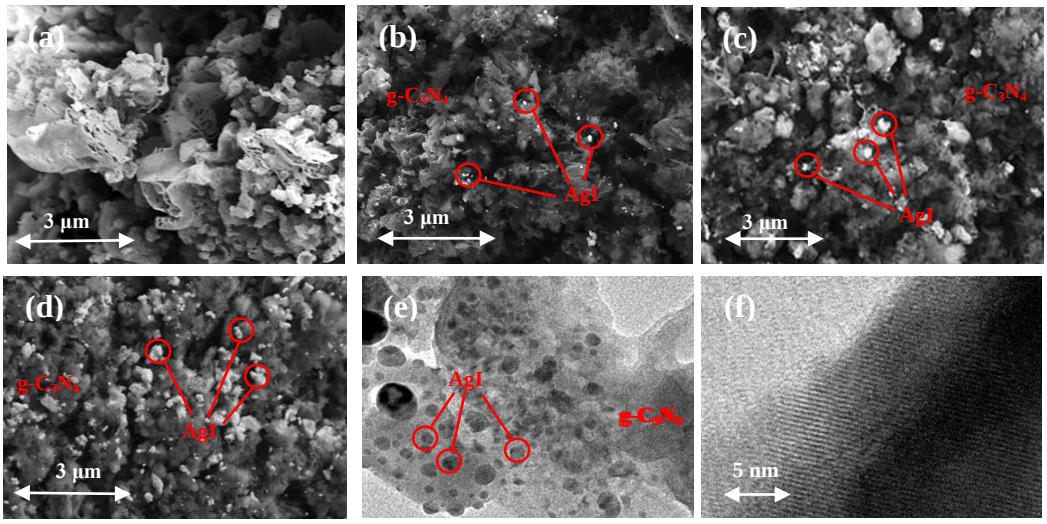


**Figure 4.** FESEM images of (a) g-$C_3N_4$ (b) 1Ag/AgI/g-$C_3N_4$ (c) 10Ag/AgI/g-$C_3N_4$ (d) 50Ag/AgI/g-$C_3N_4$, TEM images of (e)10Ag/AgI/g-$C_3N_4$ and (f) HRTEM image of 10 Ag/AgI/g-$C_3N_4$.

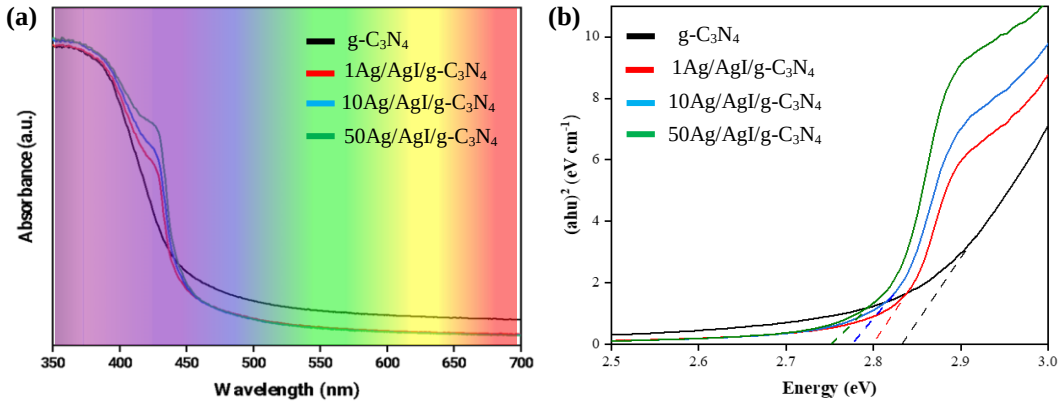


**Figure 5.** (a) UV-Vis diffuse reflectance spectra (b) Tauc plot of g-$C_3N_4$, 1Ag/AgI/g-$C_3N_4$, 10Ag/AgI/g-$C_3N_4$ and 50Ag/AgI/g-$C_3N_4$ photocatalysts.

By measuring the gradient of the Tauc plot, we can determine the value of the optical bandgap energy [45]. The Tauc plot of the synthesized samples is shown in **Figure 5(b)**. The band gap of pristine g-$C_3N_4$, 1Ag/AgI/g-$C_3N_4$, 10Ag/AgI/g-$C_3N_4$, and 50Ag/AgI/g-$C_3N_4$ are 2.83 eV, 2.80 eV, 2.77 eV and 2.75 eV, respectively. The band gap of the Ag/AgI/g-$C_3N_4$ composite photocatalysts is further reduced due to the significant amount of surface contact between Ag/AgI and g-$C_3N_4$, resulting in an effective heterojunction structure that reduces the bandgap of the photocatalysts. This structure improves photocatalytic efficacy by increasing the number of active reaction sites and facilitating charge carrier separation and transport [46].

**Figure 6** illustrates the XPS spectra of the 10Ag/AgI/g-$C_3N_4$ sample. The survey indicates that the composite photocatalyst is constructed by Ag, I, C, O, and N elements. **Figures 6(b)-(f)** depicts the deconvolution spectra of C 1s, Ag 3d, O 1s, N 1s, and I 3d. C 1s spectrum exhibited two convolution peaks at 282.42 eV and 285.76 eV that could be associated with carbide and sp2 hybridized C-N group, respectively [3,47]. The XPS spectra of Ag species display two peaks at approximately 367.19 eV and 373.18 eV, corresponding to the binding energies of $3d_{5/2}$ and $3d_{3/2}$ of $Ag^+$ [4]. This result indicates that the main chemical valence of Ag in the AgI/g-$C_3N_4$ photocatalyst sample is +1 [35]. **Figure 6(d)** shows one oxygen species corresponding to the peak at 530.7 eV attributed to the OH group [48]. The peaks for N 1s spectrum at 397.14 eV and 397.81 eV could be assigned to attributing to N sp2-bonded to two carbon atoms (C-N=C) [49]. Furthermore, the peaks at 399.49 eV and 404.35 eV are referring to tertiary N(N-$(C)_3$ and the charging effect caused by excitation [50]. The XPS spectrum of I 3d implies that the binding energies of I $3d_{3/2}$ and I $3d_{5/2}$ are 629.96 and 618.85 belonging to $I^-$, respectively [38]. The results indicated that AgI was present on the surface of g-$C_3N_4$ [39].

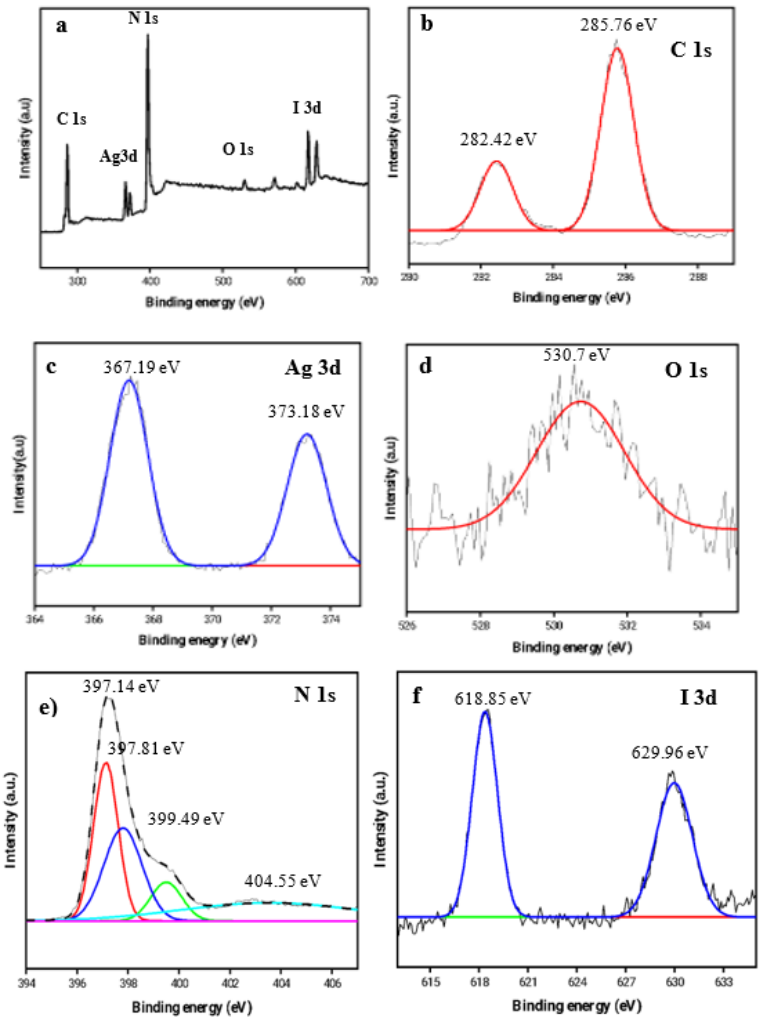


**Figure 6.** (a) XPS survey spectrum and deconvolution of (b) C 1s region (c) Ag 3d region (d) O s region (e) N 1s region (f) I 3d spectra of the 10Ag/AgI/g-$C_3N_4$ photocatalyst sample.

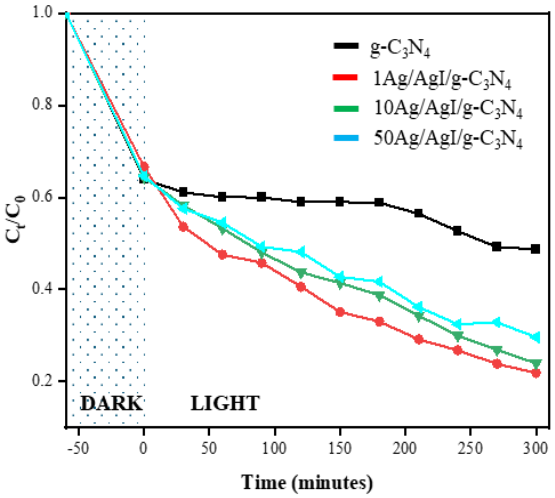


**Figure 7.** Photocatalytic activity of the synthesized photocatalyst under visible light irradiation.

**Photocatalytic Testing**

**Figure 7** depicts the change in MB concentration during the photodegradation under LED light illumination.

Initially, the reaction was performed in the dark, and all samples showed more than 40% adsorption. When the light is turned on, only 50% of the MB is degraded in 5 hours when pristine g-$C_3N_4$ is used as a photocatalyst. All Ag/AgI/g-$C_3N_4$ composites photocatalysts showed much better photocatalytic activity, with over 70% of MB being degraded within the same period, demonstrating the superior efficiency of these composites as visible-light-driven photocatalysts. The pristine g-$C_3N_4$ shows limited ability in degrading the MB due to poor visible light response and rapid recombination rate of the electron and hole. All the Ag/AgI/g-$C_3N_4$ composites show better photocatalytic activity attributed to efficient absorption of visible light and enhanced charge separation due to the synergic effect between AgI and g-$C_3N_4$ [4]. The improvement in photocatalytic ability is also due to the heterojunction system form between the AgI and g-$C_3N_4$, as observed in the TEM image (**Figure 4(e)**). This improved photocatalytic performance is also due to the LSPR effect of the Ag particle [10]. Interestingly, the photocatalytic activity of the composite catalysts decreased as the % AgI loading increased. Excessive AgI loading on the surface of g-$C_3N_4$ results in the formation of agglomeration which will shied the active sites in the system and may facilitate charge carrier recombination and ultimately reduce photocatalytic efficiency [10]. The agglomeration of AgI on the g-$C_3N_4$ surface as the % AgI loading increased, can be observed clearly in the FESEM image (Figure 4(b)-(d)). This finding agrees with a previous study done by Huang et al. [35] and Cheng et al. [39], in which the photocatalytic activity significantly increases with AgI by up to 30%. They also mentioned that the excessive AgI loading, which is the result of the aggregation of Ag/AgI nanoparticles, can be attributed to this phenomenon, as it shields the active sites in the system.

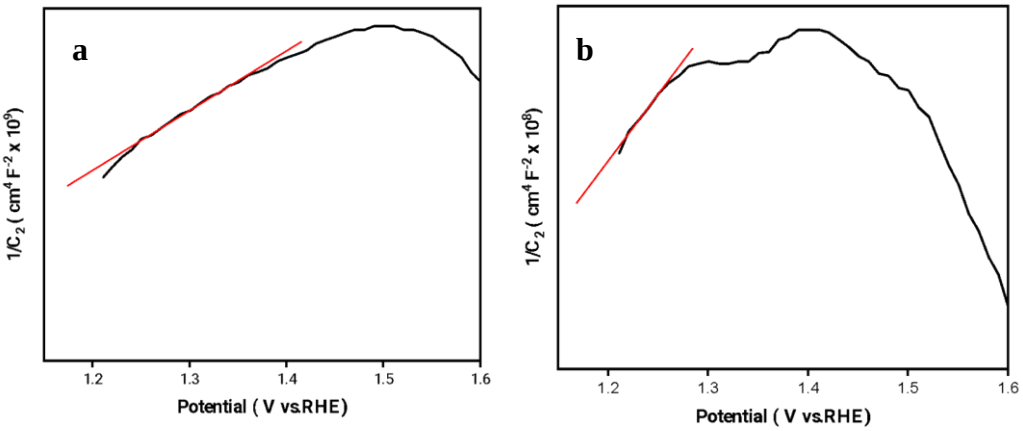


**Figure 8.** Mott-Schottky plots of (a) g-$C_3N_4$ (b) 10Ag/AgI/g-$C_3N_4$.

**Reaction Mechanism**

To comprehend how the photocatalytic reaction between the methylene blue and the Ag/AgI/g-$C_3N_4$ photocatalysts is improved, the conduction band ($E_{CB}$) and valence band ($E_{VB}$) positions of the components were determined. Mott-Schottky (M-S) plots were used to determine the flat band potential vs RHE of the g-$C_3N_4$ and the Ag/AgI/ g-$C_3N_4$ photocatalysts. The Mott-Schottky plots displayed in **Figure 8**, shows that both g-$C_3N_4$ have positive slopes, suggesting that they are n-type semiconductors [51].

From the M-S plots, the flat band ($E_{fb}$) potential vs RHE of g-$C_3N_4$ and Ag/AgI/ g-$C_3N_4$ are 0.4819 V and 0.4716 V, respectively. The flat band $E_{fb}$ potential vs RHE of g-$C_3N_4$ was then converted to $E_{fb}$ vs Ag/AgCl using the following Equations (2-5) [52]:

$$E_{fb}\,(\text{vs RHE}) = E_{fb}\,(\text{vs Ag/AgCl}) + E^{o}_{Ag/AgCl} + 0.0591\ \text{V} \times \text{pH} \quad (2)$$

$$E_{fb}\,(\text{vs NHE}) = E\,(\text{vs Ag/AgCl}) + E^{o}\,A_{g/AgCl} \quad (3)$$

$$E^{o}_{\ Ag/AgCl} = 0.1976\ \text{V vs NHE at 25 °C and pH = 6.9}) \quad (4)$$

Thus, the corresponding $E_{fb}$ vs Ag/AgCl of the g-$C_3N_4$ and Ag/AgI/ g-$C_3N_4$ are -0.12219 V and -0.1324 V. Utilizing the connection where the $E_{CB}$ is -0.1 V or 0.2 V more negative than the $E_{fb}$ for n-type semiconductor [53], the $E_{CB}$ was found to be –0.32 V and -0.33 V for g-$C_3N_4$ and Ag/AgI/ g-$C_3N_4$, respectively. When converted to the normal hydrogen electrode (NHE) scale where:

$$E_{CB}\ \text{vs NHE} = E_{CB}\ \text{vs Ag/AgCl} + 0.197\ \text{V [54],} \quad (5)$$

the values became -0.12 V (for g-$C_3N_4$) and -0.13 V (for Ag/AgI/ g-$C_3N_4$). According to the equation $E_{VB} = E_{CB} + E_g$ where $E_g$ is band gap energy [55], the $E_{VB}$ was calculated to be 2.71 V for g-$C_3N_4$ and 2.64 V for g-$C_3N_4$/Ag/AgI.

The reaction mechanism is postulated to comprehend the improved photocatalytic performance of the Ag/AgI/g-$C_3N_4$ composite photocatalyst. The suggested mechanism is displayed in **Figure 9**.

When exposed to light, both AgI and g-$C_3N_4$ produce electrons and holes. The Ag nanoparticles absorb light and provide photogenerated electrons via the surface plasmon resonance effect. The electrons from the Ag nanoparticles are injected into the $E_{CB}$ of g-$C_3N_4$ due to their favorable alignment, thereby enhancing electron density in g-$C_3N_4$. Then, electrons in the $E_{CB}$ of AgI can transfer to the $E_{CB}$ of g-$C_3N_4$ due to the close alignment of their $E_{CB}$ energies. The photogenerated charge carriers are effectively separated through this process, which enhances the photocatalytic reactivity of Ag/AgI/g-$C_3N_4$ composite photocatalysts. The photogenerated electrons in the $E_{CB}$ of g-$C_3N_4$ react with dissolved oxygen ($O_2$) to produce reactive oxygen species (ROS) such as superoxide radicals ($^{\cdot}O_2^{-}$), which contribute to the degradation of methylene blue. The holes (h+) in $E_{VB}$ of g-$C_3N_4$ and AgI can oxidize water or hydroxyl ions ($OH^{-}$) to form hydroxyl radicals ($^{\cdot}OH$) which will further degrade the methylene blue.

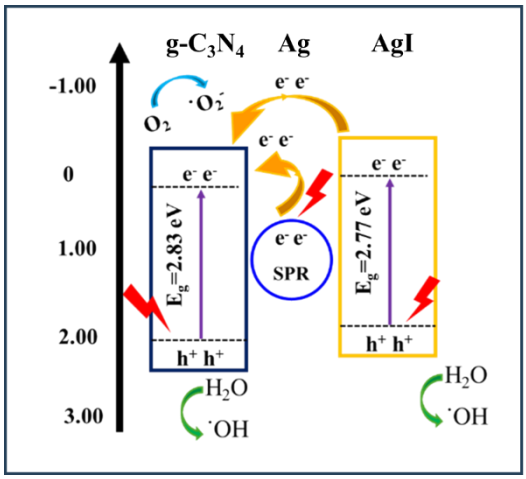


**Figure 9.** Proposed photocatalytic mechanism of Ag/AgI/g-$C_3N_4$ composite photocatalyst.

**Table 1**. Comparative of degradation efficiency for MB using different photocatalysts.

| Samples | Light Source | Degradation Efficiency (%) | References |
|---|---|---|---|
| g-$C_3N_4$/$Ca_2Fe_2O_5$ | Natural sunlight | 95.4 (70 min) | [56] |
| ZnO-NR/ACF nanocomposites | UV irradiation | 99 (120 min) | [57] |
| 70% $CeO_2$/g-$C_3N_4$ | UV light irradiation | 90.1 (180 min) | [58] |
| β-$Cu_2V_2O_7$/$Zn_2V_2O_6$ | 300 Xenon Lamp | 98.7 (65 min) | [59] |
| 5% PTh/ZnO | 250 W high-pressure mercury lamp | 95 (180 min) | [60] |
| γ-$Fe_3$/$Fe_3O_4$/$SiO_2$ (Ar modified) | UV light | 87.5 (120 min) | [61] |

## COMPARISON WITH OTHER PHOTOCATALYSTS

**Table 1** compares the MB degradation efficiency with different photocatalysts reported in the literature. While Ag/AgI/g-$C_3N_4$ was used in this work, it was able to degrade MB by approximately 80% within 5 hours under visible light illumination. The value for degradation efficiency in the present work is significantly considerable compared to most other photocatalysts reported. Thus, the current work showed that adding Ag and AgI improved the ability to absorb visible light and separate electrons and holes, which led to better photocatalytic performance.

## CONCLUSION

Using a straightforward in-situ co-precipitation technique, a range of visible light responsive Ag/AgI/g-$C_3N_4$ photocatalysts were successfully fabricated. The resulting Ag/AgI/g-$C_3N_4$ composite photocatalysts demonstrated increased photocatalytic efficiency toward methylene blue dye when exposed to visible light. The 1 percent AgI loading composite degraded 80% of MB in 5 hours, which is almost two times than the g-$C_3N_4$. In contrast to the pristine g-$C_3N_4$, the incorporation of Ag and AgI enhanced visible-light absorption and electron-hole separation, leading to better photocatalytic performance. In summary, the synergistic effects of Ag, AgI, and g-$C_3N_4$ formed a stable heterojunction and utilized the Ag localized surface plasmon resonance (LSPR) effect to provide the improved photocatalytic efficiency of the Ag/AgI/g-$C_3N_4$ composite photocatalysts.

## ACKNOWLEDGEMENTS

We wish to extend our appreciation to the Universiti Teknologi MARA (UiTM) for their support under the Strategic Research Partner (SRP) grant with Qatar University with project no. 100-RMC 5/3/SRP (005/2023).

## REFERENCES

1. Nawaz, A., Naz, I., Atif, M., Khan, A. and Ali, N. (2023) Preparation and characterization of single perovskite microplates and its sunlight assisted photodecolorization activity, validated by response surface methodology. *Chemosphere*, **334,** 138923.

2. Du, R., Xiao, K., He, S., Wang, Y. and Kang, C. (2023) Constructing of 3D flower-like $MoS_2$/$Bi_4Ti_3O_{12}$ p-n heterojunction for the enhancement of photocatalytic degradation of dyes. *Journal of Alloys and Compounds*, **955**, 170168.

3. Liu, L., Qi, Y., Yang, J., Cui, W., Li, X. and Zhang, Z. (2015) An AgI@g-$C_3N_4$ hybrid core@shell structure: Stable and enhanced photocatalytic degradation. *Applied Surface Science*, **358**, 319–327.

4. Lei, C., Pi, M., Zhu, X., Xia, P., Guo, Y. and Zhang, F. (2016) Highly efficient visible-light photocatalytic performance based on novel AgI/g-$C_3N_4$ composite photocatalysts. *Chemical Physics Letters*, **664**, 167–172.

5. Xu, H., Yan, J., Xu, Y., Song, Y., Li, H., Xia, J., Huang, C. and Wan, H. (2013) Novel visible-light-driven AgX/graphite-like $C_3N_4$ (X=Br, I) hybrid materials with synergistic photocatalytic activity. *Applied Catalysis B: Environmental*, **129**, 182–193.

6. Yang, L., Gao, M., Dai, B., Guo, X., Liu, Z. and Peng, B. (2016) Synthesis of spindle-shaped AgI/TiO 2 nanoparticles with enhanced photocatalytic performance. *Applied Surface Science*, **386,** 337–344.

7. Guo, J. F., Ma, B., Yin, A., Fan, K. and Dai, W. L. (2011) Photodegradation of rhodamine B and 4-chlorophenol using plasmonic photocatalyst of Ag-AgI/$Fe_3O_4$@$SiO_2$ magnetic nanoparticle under visible light irradiation. *Applied Catalysis B: Environmental*, **101,** 580–586.

8. Xie, X., Wang, S., Zhang, Y., Ding, J., Liu, Y., Yan, Q., Lu, S., Li, B., Liu, Y. and Cai, Q. (2021) Facile construction for new core-shell Z-scheme photocatalyst GO/AgI/$Bi_2O_3$ with enhanced visible-light photocatalytic activity. *Journal of Colloid Interface Science*, **581,** 148–158.

9. Tian, L., Li, J., Wang, J., Yang, Z., Li, Y., Zhang, L. and Zhang, G. (2024) Built-in electric field intensified by SPR effect to drive charge separation over Ag-AgI/$Sb_2S_3$ heterojunction for high-efficiency photocatalytic metronidazole mineralization. *Separation and Purification Technology*, **346,** 127443.

10. Bai, C., Bi, J., Wu, J., Xu, Y., Wohlrab, S., Han, Y. and Zhang, X. (2019) In- situ solid-phase fabrication of Ag/AgX (X=Cl, Br, I)/g-$C_3N_4$ composites for enhanced visible-light hydrogen evolution. *International Journal of Hydrogen Energy*, **44,** 21397–21405.

11. Zeng, H., Liu, Y., Xu, Z., Wang, Y., Chai, Y., Yuan, R. and Liu, H. (2019) Construction of a Z-scheme g-$C_3N_4$/Ag/AgI heterojunction for highly selective photoelectrochemical detection of hydrogen sulfide. *Chemical Communications*, **55,** 11940–11943.

12. Dong, G., Zhang, Y., Pan, Q. and Qiu, J. (2014) A fantastic graphitic carbon nitride (g-$C_3N_4$) material: Electronic structure, photocatalytic and photoelectronic properties. *Journal of Photochemistry and Photobiology C: Photochemistry Reviews*, **20,** 33–50.

13. Wei, F., Liu, Y., Zhao, H., Ren, X., Liu, J., Hasan, T., Chen, L., Li, Y. and Su, B. L., (2018) Oxygen self-doped g-$C_3N_4$ with tunable electronic band structure for unprecedentedly enhanced photocatalytic performance. *Nanoscale*, **10,** 4515–4522.

14. Le, S., Zhu, C., Cao, Y., Wang, P., Liu, Q., Zhou, H., Chen, C., Wang, S. and Duan, X. (2022) $V_2O_5$ nanodot-decorated laminar $C_3N_4$ for sustainable photodegradation of amoxicillin under solar light. *Applied Catalysis B: Environmental*, **303,** 120903.

15. Velmurugan, S., Balu, S., Palanisamy, S., Yang, T. C. K., Velusamy, V., Chen, S. W. and El-Shafey, E. S. I. (2020) Synthesis of novel and environmental sustainable AgI-$Ag_2S$ nanospheres impregnated g-$C_3N_4$ photocatalyst for efficient degradation of aqueous pollutants. *Applied Surface Science*, **500,** 143991.

16. Yang, Y., Jin, H., Zhang, C., Gan, H., Yi, F. and Wang, H. (2020) Nitrogen-deficient modified P–Cl co-doped graphitic carbon nitride with enhanced photocatalytic performance. *Journal of Alloys and Compounds*, **821,** 153439.

17. Chandel, N., Sharma, S., Dutta, V., Raizada, P., Hosseini-Bandegharaei, A., Kumar, R., Gupta, V. K., Agarwal, S. and Singh, P. (2020) Adsorption and photocatalysis compiled toxic dyes mineralization using graphitic carbon nitride modified $ZnFe_2O_4$ and $CoFe_2O_4$ photocatalysts supported onto N-doped graphene. *Desalination and Water Treatment*, **191,** 381–399.

18. Bao, J., Bai, W., Wu, M., Gong, W., Yu, Y., Zheng, K. and Liu, L. (2022) Template-mediated copper doped porous g-C3N4 for efficient photodegradation of antibiotic contaminants. *Chemosphere*, **293,** 133607.

19. Xu, F., An, N., Lai, C., Zhang, M., Li, B., Liu, S., Li, L., Qin, L., Fu, Y., Yi, H. and Yan, H. (2022) Nitrogen-doping coupled with cerium oxide loading co-modified graphitic carbon nitride for highly enhanced photocatalytic degradation of tetracycline under visible light. *Chemosphere*, **293,** 133648.

20. Bai, X., Li, M., Li, J., Rao, X., Zheng, S. and Zhang, Y. (2021) Graphitic Carbon Nitride Codoped with Sulfur and Yttrium for Efficient Visible-Light Photocatalytic Performance. *ACS Applied Energy Materials*, **4(12),** 14390–14399.

21. Hassanzadeh-Tabrizi, S. A. (2021) Synthesis of $NiFe_2O$/Ag nanoparticles immobilized on mesoporous g-$C_3N_4$ sheets and application for degradation of antibiotics. *Journal of Photochemistry and Photobiology A: Chemistry*, **418,** 120903.

22. Van Thuan, D., Nguyen, T. L., Pham Thi, H. H., Thanh, N. T., Ghotekar, S., Sharma, A. K., Binh, M. T., Nga, T. T., Pham, T. D. and Cam, D. P. (2022) Development of Indium vanadate and Silver deposited on graphitic carbon nitride ternary heterojunction for advanced photocatalytic degradation of residual antibiotics in aqueous environment. *Optical Materials*, **123,** 1–6.

23. Ong, W. J., Putri, L. K., Tan, L. L., Chai, S. P. and Yong, S. T. (2016) Heterostructured AgX/g-$C_3N_4$ (X=Cl and Br) nanocomposites via a sonication-assisted deposition-precipitation approach: Emerging role of halide ions in the synergistic photocatalytic reduction of carbon dioxide. *Applied Catalysis B: Environmental*, **180,** 530–543.

24. Du, J., Xu, N., Yuan, P., Shu, Q., Wang, C., Xu, Q., Zhang, P., Zhuo, S. and Zhu, C. (2023) Designing ultrathin Ag-embedded g-$C_3N_4$ nanocomposites for enhanced disinfection performance under visible light. *Journal of Molecular Structure*, **1276**, 134810.

25. Suyana, P., Ganguly, P., Nair, B. N., Pillai, S. C. and Hareesh, U. S. (2021) Structural and compositional tuning in g-$C_3N_4$ based systems for photocatalytic antibiotic degradation. *Chemical Engineering Journal Advances*, **8**, 100148.

26. Waheed, I. F., Hamad, M. A., Jasim, K. A. and Gesquiere, A. J. (2023) Degradation of methylene blue using a novel magnetic $CuNiFe_2O_4$/g-$C_3N_4$ nanocomposite as heterojunction photocatalyst. *Diamond and Related Materials*, **133**, 109716.

27. Wang, W., Li, Z., Wu, K., Dai, G., Chen, Q., Zhou, L., Zheng, J., Ma, L., Li, G., Wang, W. and An, T. (2023) Novel Ag-bridged dual Z-scheme g-$C_3N_4$/ BiOI/AgI plasmonic heterojunction: Exceptional photocatalytic activity towards tetracycline and the mechanism insight. *Journal of Environmental Sciences*, **131**, 123–140.

28. Li, Y., Gu, M., Zhang, X., Fan, J., Lv, K., Carabineiro, S. A. C. and Dong, F. (2020) 2D g-$C_3N_4$ for advancement of photo-generated carrier dynamics: Status and challenges. *Materials Today*, **41**, 270–303.

29. Lu, Z., Zeng, D., Zheng, H., Liu, Q., Gao, X., He, X., Wei, L. and Ong, W. J. (2020) Enhanced interfacial electron transfer and boosted visible-light photocatalytic hydrogen evolution activity of g-$C_3N_4$ by noble-metal-free $MoSe_2$ nanoparticles. *Journal of Materials Science*, **55(27)**, 13114–13126.

30. Tran, V. H. T., Huynh, T. C. and Pham, V. Van (2021) The effect of excitation light source and humidity to photocatalytic activity of g-$C_3N_4$ nano-sheets for NO removal. *Science and Technology Development Journal*, **24(2)**, 1924–1932.

31. Morsy, M., Gomaa, I., Mokhtar, M. M., ElHaes, H. and Ibrahim, M. (2023) Design and implementation of humidity sensor based on carbon nitride modified with graphene quantum dots. *Scientific Reports*, **13(1)**, 1–18.

32. Huang, H., Wang, H. L. and Jiang, W. F. (2023) In-situ synthesis of novel dual S-scheme AgI/ $Ag_6Mo_7O_{24}$/g-$C_3N_4$ heterojunctions with tandem structure for photocatalytic degradation of organic pollutants. *Chemosphere*, **318**, 137812.

33. Wang, L., Hou, Y., Xiao, S., Bi, F., Zhao, L., Li, Y., Zhang, X., Gai, G. and Dong, X. (2019) One-step, high-yield synthesis of g-$C_3N_4$ nanosheets for enhanced visible light photocatalytic activity. *RSC Advances*, **9(67)**, 39304–39314.

34. Zhang, Wendong, Zhang, Q., Dong, F. and Zhao, Z. (2013) The multiple effects of precursors on the properties of polymeric carbon nitride. *International Journal of Photoenergy*, **2013**, 1–9.

35. Huang, H., Li, Y. X., Wang, H. L. and Jiang, W. F. (2021) In situ fabrication of ultrathin-g-$C_3N_4$/ AgI heterojunctions with improved catalytic performance for photodegrading rhodamine B solution. *Applied Surface Science*, **538**, 148132.

36. Mehtab, A., Alshehri, S. M. and Ahmad, T. (2022) Photocatalytic and Photoelectrocatalytic Water Splitting by Porous g-$C_3N_4$Nanosheets for Hydrogen Generation. *ACS Applied Nano Materials*, **5**, 12656–12665.

37. Cui, L., Pu, T., Fang, X., Song, J., Li, S., Wang, J., Yin, C., Shi, H. and Kang, S. (2018) Graphitic Carbon Nitride Sputtered with Silver Nanoparticles for Efficient Photocatalytic Degradation of Rhodamine B Dye. *International Journal of Electrochemical Science*, **13**, 4981–4990.

38. Zhang, J., Zhu, Z., Jiang, J. and Li, H. (2020) Ultrasound-Assisted Hydrothermal Fabrication of Sheet – Sphere – Sheet Photocatalysts with Enhanced. *Catalysts*, **4**, 373.

39. Cheng, Y., He, L., Xia, G., Ren, C. and Wang, Z. (2019) Nanostructured g-$C_3N_4$/AgI composites assembled by AgI nanoparticles-decorated g-$C_3N_4$ nanosheets for effective and mild photooxidation reaction. *New Journal of Chemistry*, **43**, 14841–14852.

40. Wang, W., Li, Z., Wu, K., Dai, G., Chen, Q., Zhou, L., Zheng, J., Ma, L., Li, G., Wang, W. and An, T. (2023) Novel Ag-bridged dual Z-scheme g-$C_3N_4$/ BiOI/AgI plasmonic heterojunction: Exceptional photocatalytic activity towards tetracycline and the mechanism insight. *Journal of Environmental Sciences*, **131**, 123–140.

41. Tang, M., Ao, Y., Wang, C. and Wang, P. (2020) Facile synthesis of dual Z-scheme g-$C_3N_4$/$Ag_3PO_4$/ AgI composite photocatalysts with enhanced performance for the degradation of a typical neonicotinoid pesticide. *Applied Catalysis B: Environmental*, **268**, 118395.

42. Bai, C., Bi, J., Wu, J., Xu, Y., Wohlrab, S., Han, Y. and Zhang, X. (2019). In- situ solid-phase fabrication of Ag/AgX (X=Cl, Br, I)/g-$C_3N_4$ composites for enhanced visible-light hydrogen evolution. *International Journal of Hydrogen Energy*, **44**, 21397–21405.

43. Zhang, W., Zhou, L., Shi, J. and Deng, H. (2017) Fabrication of novel visible-light-driven AgI/g-$C_3N_4$ composites with enhanced visible-light photocatalytic activity for diclofenac degradation. *Journal of Colloid and Interface Science*, **496**, 167–176.

44. Olusegun, S. J., Larrea, G., Osial, M., Jackowska, K. and Krysinski, P. (2021) Photocatalytic degradation of antibiotics by superparamagnetic iron oxide nanoparticles. Tetracycline case. *Catalysts*, **11**, 1243.

45. Sánchez-Vergara, M. E., Alonso-Huitron, J. C., Rodriguez-Gómez, A. and Reider-Burstin, J. N. (2012) Determination of the optical GAP in thin films of amorphous dilithium phthalocyanine using the Tauc and Cody models. *Molecules*, **17**, 10000–10013.

46. Zhang, X., Ren, B., Li, X., Xu, Y., Liu, B., Yu, P., Sun, Y. and Mei, D. (2021) Efficiently enhanced visible-light photocatalytic activity by in situ deposition of Ag@AgBr on g-$C_3N_4$/$Fe_3O_4$ magnetic heterogeneous materials. *Separation and Purification Technology*, **254**, 117596.

47. Gieroba, B., Sroka-Bartnicka, A., Kazimierczak, P., Kalisz, G., Lewalska-Graczyk, A., Vivcharenko, V., Nowakowski, R., Pieta, I. S. And Przekora, A. (2020) Spectroscopic studies on the temperature-dependent molecular arrangements in hybrid chitosan/1,3-β-D-glucan polymeric matrices. *International Journal of Biological Macromolecules*, **159**, 911–921.

48. Yang, G., Wang, L., Zheng, S., Wu, H., Hao, D., Li, Q., Du, H., Yamashita, H. and Wang, Q. (2023) Novel dual Z-scheme Ag-bridged AgI/$FeVO_4$-$C_3N_4$ plasmonic heterojunction: A study on the performance and mechanism of photocatalytic reduction of Cr(VI). *Journal of Environmental Chemical Engineering*, **11**, 110071.

49. Tang, H., Chang, S., Tang, G. and Liang, W. (2017) AgBr and g-$C_3N_4$ co-modified $Ag_2CO_3$ photocatalyst: A novel multi-heterostructured photocatalyst with enhanced photocatalytic activity. *Applied Surface Science*, **391**, 440–448.

50. Xu, W., Lai, S., Pillai, S. C., Chu, W., Hu, Y., Jiang, X., Fu, M., Wu, X., Li, F. and Wang, H. (2020) Visible light photocatalytic degradation of tetracycline with porous Ag/graphite carbon nitride plasmonic composite: Degradation pathways and mechanism. *Journal of Colloid and Interface Science*, **574**, 110–121.

51. Meng, A., Cheng, B., Tan, H., Fan, J., Su, C. and Yu, J. (2021) $TiO_2$/polydopamine S-scheme heterojunction photocatalyst with enhanced $CO_2$ -reduction selectivity. *Applied Catalysis B: Environmental*, **289**, 120039.

52. Ma, Y., Zhang, Z., Jiang, X., Sun, R., Xie, M. and Han, W. (2021) Direct Z-scheme Sn-$In_2O_3$/$In_2S_3$ heterojunction nanostructures for enhanced photocatalytic $CO_2$ reduction activity. *Journal of Materials Chemistry C*, **9**, 3987–3997.

53. Li, X., Yu, J., Low, J., Fang, Y., Xiao, J. and Chen, X. (2015) Engineering heterogeneous semiconductors for solar water splitting. *Journal of Materials Chemistry A*, **3**, 2485–2534.

54. Yi, S. S., Yan, J. M., Wulan, B. R., Li, S. J., Liu, K. H. and Jiang, Q. (2017) Noble-metal-free cobalt phosphide modified carbon nitride: An efficient photocatalyst for hydrogen generation. *Applied Catalysis B: Environmental*, **200,** 477–483.

55. Liu, K., Wang, X., Li, C., Gao, M., Cao, N., Zhao, X., Li, W., Ding, X., Li, Z., Du, X. and Feng, J. (2022). Facile fabrication metal Cu-decorated g-$C_3N_4$ photocatalyst with Schottky barrier for efficient pollutant elimination. *Diamond and Related Materials*, **126**, 109116.

56. Vavilapalli, D. S., Peri, R. G., Sharma, R. K., Goutam, U. K., Muthuraaman, B., Ramachandra Rao, M. S. and Singh, S. (2021) g-$C_3N_4$/$Ca_2Fe_2O_5$ heterostructures for enhanced photocatalytic degradation of organic effluents under sunlight. *Scientific Reports*, **11**, 1–11.

57. Albiss, B., & Abu-Dalo, M. (2021) Photocatalytic degradation of methylene blue using zinc oxide nanorods grown on activated carbon fibers. *Sustainability*, **13**, 4729.

58. Wei, X., Wang, X., Pu, Y., Liu, A., Chen, C., Zou, W., Zheng, Y., Huang, J., Zhang, Y., Yang, Y., Naushad, M., Gao, B. And Dong, L. (2021) Facile ball-milling synthesis of $CeO_2$/g-$C_3N_4$ Z-scheme heterojunction for synergistic adsorption and photo-degradation of methylene blue: Characteristics, kinetics, models, and mechanisms. *Chemical Engineering Journal*, **420**, 127719.

59. Ashraf, M., Khan, I., Baig, N., Hendi, A. H., Ehsan, M.F. and Sarfraz, N. (2021) A Bifunctional 2D Interlayered β-$Cu_2V_2O_7$/$Zn_2V_2O_6$(CZVO) Hetero-junction for Solar-Driven Nonsacrificial Dye Degradation and Water Oxidation. *Energy Technology*, **9**, 2100034.

60. Faisal, M., Harraz, F. A., Jalalah, M., Alsaiari, M., Al-Sayari, S. A. and Al-Assiri, M. S. (2020) Polythiophene doped ZnO nanostructures synthesized by modified sol-gel and oxidative polymerization for efficient photodegradation of methylene blue and gemifloxacin antibiotic. *Materials Today Communications*, **24**, 101048.

61. Sanad, M. M. S., Farahat, M. M., El-Hout, S. I. and El-Sheikh, S. M. (2021) Preparation and characterization of magnetic photocatalyst from the banded iron formation for effective photodegradation of methylene blue under UV and visible illumination. *Journal of Environmental Chemical Engineering*, **9**, 105127.